Marine Pollution Bulletin 207 (2024) 116888

Contents lists available at ScienceDirect

Marine Pollution Bulletin

journal homepage: www.elsevier.com/locate/marpolbul

Marine debris induced by the Great East Japan Earthquake and Tsunami: A multi-sensor remote sensing assessment

Lin Qi [a,b,*], Menghua Wang [a], Chuanmin Hu [c], Junnan Jiao [c], Young-Je Park [d]

[a] NOAA Center for Satellite Applications and Research, College Park, 5830 University Research Court, College Park, MD 20740, USA
[b] Global Science & Technology Inc., 7501 Greenway Center Drive #1100, Greenbelt, MD 20770, USA
[c] College of Marine Science, University of South Florida, 140 Seventh Avenue South, St. Petersburg, Florida 33701, USA
[d] TelePIX Co. Ltd., 2 Gukjegeumyung-ro 8-gil, Yeongdeungpo-gu, Seoul 07330, Republic of Korea

ARTICLE INFO

Keywords:
The Great East Japan Earthquake
Tsunami
The Japanese Tsunami Marine Debris
Plastics
Marine hazards
Remote sensing
Marine debris

ABSTRACT

Using satellite remote sensing, we show the distribution, dominant type, and amounts of marine debris off the northeast coast of Japan after the Great East Japan Earthquake on 11 March 2011 and subsequent tsunami. Extensive marine debris was found on March 12, with the maximal amount found on March 13. The debris was found to be mainly wood (possibly lumber wood), with an estimated 1.5 million metric tons in an elongated water area of 6800 km^2 (18 km E-W and 380 km N-S) near parallel to the coast between 36.75°N and 40.25°N. The amount decreased rapidly with time, with scattered debris patches captured in high-resolution satellite images up to April 6. These results provide new insights on the initial distribution of the Japanese Tsunami Marine Debris, which may be used to help find bottom deposition of debris and help refine numerical models to predict the debris trajectory and fate.

Synopsis: Marine debris induced by the 2011 Great East Japan Earthquake and Tsunami is found to be mainly composed of wood and possibly lumber wood from constructions, with maximum amount on 13 March 2011 distributed within a narrow band of ~18 km near parallel to the northeast coast of Japan between 36.75°N and 40.25°N.

1. Introduction

Tsunamis can cause tremendous damage and large amounts of debris (e.g., plastics, damaged boats and houses, lumber wood and other wood, fishing gears, clothes, and other materials) released to the ocean. Following ocean circulations, such marine debris (a.k.a. marine litter) can be dissipated over extremely large scales (Murray et al., 2018a), which represents an environmental hazard and may have detrimental impacts on marine ecology (Law et al., 2010; Cózar et al., 2014; Eriksen et al., 2014; MacLeod et al., 2021). In particular, marine debris of anthropogenic origin is known to cause adverse impacts on reptiles (Staffieri et al., 2019), marine mammals (Poeta et al., 2017), and seabirds (Battisti et al., 2019). The 2011 tsunami off the northeast coast of Japan, induced by the Great East Japan Earthquake, sets an example on how large amounts of debris of various types from damaged houses and other properties can travel across the entire North Pacific to reach Hawaii as well as the west coast of California (U.S.) and Vancouver (Canada), with measurable impacts on biology and ecology, as well as on beach pollutions (Murray et al., 2018a, 2018b). For example, at least 7 of the ~370 species of invertebrates, algae, and fish identified from the debris were new or non-indigenous to coastal ecosystems around Hawaii and in North America (Carlton et al., 2017, 2018; Hanyuda et al., 2018). Some of these invaders represented high risk to local ecosystems (Therriault et al., 2018).

At a magnitude of 9.0–9.1 Mw, the Great East Japan Earthquake occurred on 11 March 2011 (05:46:24 GMT) on the seafloor at 38.322°N and 142.369°E, about 70 km east of the nearest Japanese coast and 130 km east of the city of Sendai (Fig. 1 inset, Fujii et al., 2011). Known as the most powerful earthquake in the recorded Japanese history, it caused a massive tsunami with a maximum height of 40.5 m in Miyako, Iwate, Tōhoku. The tsunami caused >18,000 deaths, destroyed 300,000 buildings, and damaged >1,000,000 buildings (Suppasri et al., 2013). The Ministry of Environment of Japan estimated that ~1.5 million metric tons of debris were washed into the Pacific Ocean (Ministry of Environment of Japan (MoE), 2012), most of which were houses but the debris also contained substantial amounts of other materials such as

* Corresponding author at: NOAA Center for Satellite Applications and Research, College Park, 5830 University Research Court, College Park, MD 20740, USA.
E-mail address: lin.qi@noaa.edu (L. Qi).

https://doi.org/10.1016/j.marpolbul.2024.116888
Received 2 August 2024; Received in revised form 19 August 2024; Accepted 20 August 2024
Available online 6 September 2024

plastics.

This debris was termed as the Japanese Tsunami Marine Debris (JTMD), which was the subject of a series of studies to understand its impacts on the ocean, coastal, and beach environments along its transport pathways. As a result, a special issue of Marine Pollution Bulletin was dedicated to the targeted project to study the JTMD, entitled Assessing Debris Related Impact From Tsunami (ADRIFT), with 11 publications focused on three major themes: "1) forecasting and hindcasting JTMD trajectories and landings; 2) surveillance and detection of JTMD, and 3) characterizing and assessing the invasion risk of non-indigenous species (NIS) transported on JTMD" (Murray et al., 2018b). Interested readers may refer to the special issue to obtain more information on the JTMD itself as well as on its biological and ecological impacts (e.g., Hanyuda et al., 2018; Therriault et al., 2018).

Despite such a coordinated effort to understand the JTMD, however, the initial distribution of the JTMD after the tsunami event, specifically off the northeast coast of Japan, is understudied and largely unknown. This is possibly due to lack of resources to conduct ship-borne or airborne surveys in the extensive coastal areas after the tragic event, as some of marine debris can quickly dissipate and sink to the ocean floor. Satellite remote sensing can provide rapid, synoptic, and frequent assessment of the surface ocean, yet detecting and quantifying marine

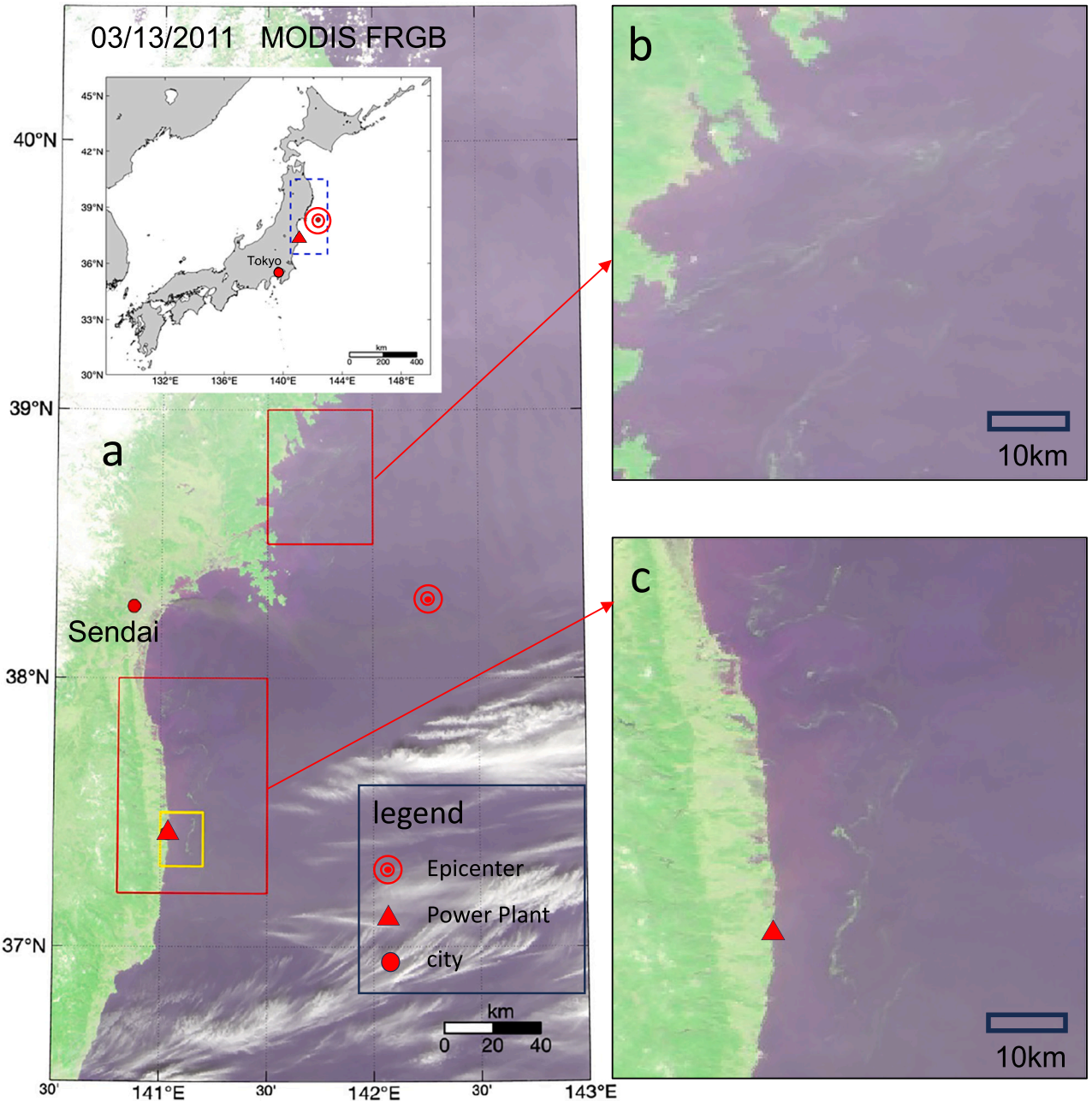

Fig. 1. An example of how marine debris appears in satellite imagery. (a) MODIS False-color Red-Green-Blue (FRGB) image collected on 13 March 2011 (03:50 GMT) off the northeast coast of Japan showing greenish image features that are determined to be marine debris (mainly wood, see below). The inset map shows the location of the MODIS image in dashed blue box as well as the epicenter of the Great Japan Earthquake (11 March 2011, 05:46:24 GMT, 38.322°N 142.369°E). The 9.0–9.1 Mw earthquake lasted for 6 min, causing a major tsunami (up to 40.5 m). The red triangle indicates the location of Fukushima Daiichi Nuclear Power Plant, which was destroyed by the tsunami. Two small areas (red boxes) are enlarged in (b) and (c), respectively, to show more details of the greenish image features. The yellow outlined region in (a) shows the coverage of high-resolution satellite image used in Matthews et al. (2017). (For interpretation of the references to color in this figure legend, the reader is referred to the web version of this article.)

debris can be technically challenging because of their small size (relative to the size of an image pixel) and other confusion factors (Hu, 2021). To date, the only two published remote sensing studies on the JTMD appear to be Arii et al. (2014) and Matthews et al. (2017), with the former focused on mapping debris using Synthetic Aperture Radar (SAR) and the latter focused on the understanding of the debris morphology (size, shape, orientation). Because of the limitations in spatial and temporal coverage of the sensors, their study regions are rather limited, with emphasis on sensor and model capacity, respectively. For example, the study of Matthews et al. (2017) was restricted to a small area off Okuma (yellow box in Fig. 1a). As a result, the initial distribution of the JTMD around Japan is still largely unknown. Such a lack of knowledge not only hinders the understanding of the fate of JTMD (e.g., where most debris sink and how ocean ecology is impacted), but also creates difficulty in initializing numerical tracers to understand the debris drift. For example, because of the unknown initial distributions of JTMD, the numerical model used in Maximenko et al. (2018) assigned number of particles in each coastal location according to the reported number of damaged houses, which may induce uncertainties when such assumptions depart from the real JTMD distributions. However, at that time, that assumption may represent the best approach to numerically track the debris drift.

Recent advances in remote sensing methodology make it possible to revisit how to map JTMD using satellite observations, with particular emphasis on passive remote sensing techniques through the use of reflected sunlight. Several papers have provided reviews on the available satellite sensors and possible methods to address the technical challenges (Martínez-Vicente et al., 2019; Topouzelis et al., 2021; Goddijn-Murphy et al., 2024), while many case studies using the Multispectral Instrument (MSI, 10–60 m resolution) onboard the Sentinel-2 satellites have been demonstrated (e.g., Themistocleous et al., 2020; Kikaki et al., 2024; Cózar et al., 2024). In principle, it is possible to first detect suspicious image features based on their spatial contrasts, and then discriminate whether they are caused by marine debris or some forms of floating vegetation based on their spectral shapes (Hu, 2021, 2022).

This strategy has been applied to medium-resolution satellite sensors to map marine debris in the northern Gulf of Mexico after the passage of Hurricane Katrina (Hu et al., 2023). Such sensors include the Moderate Resolution Imaging Spectroradiometer (MODIS, 1999–present on Terra and 2022–present on Aqua, with two 250-m bands) and the Medium Resolution Imaging Spectrometer (MERIS, 2002–2012, 300-m bands). This is particularly important because modern high-resolution satellite sensors such as MSI are not available before 2015, making MODIS and MERIS a primary choice. One limitation with these medium-resolution sensors is their lack of capacity in detecting small debris patches, but the case study of Hu et al. (2023) paves the pathway to map relatively large debris patches after natural disasters.

The objective of this work is to detect, discriminate, and quantify the JTMD using these medium-resolution multi-band satellite sensors. Of particular interest is whether the JTMD is evenly distributed along the northeast coast of Japan immediately following the tsunami.

2. Data and methods

The methodology to download and process satellite data and to detect, discriminate, and quantify marine debris has been described in Hu et al. (2023). For completeness, it is briefly described here.

Three types of satellite sensors were used in this work for different purposes: MODIS sensors were used to map and quantify marine debris because of their 250-m resolution and daily revisits with a swath width of 2330 km; MERIS with a narrower swath (1150 km) was used to spectrally discriminate the image features because of its 300-m resolution and many visible and near-infrared (NIR) bands; Landsat and ASTER (the Advanced Spaceborne Thermal Emission and Reflection Radiometer) sensors have low revisit frequency but higher resolution (30 m and 15 m respectively), therefore were used to visualize the small image features whenever images were available. An ASTER image was also used to evaluate the accuracy of the MODIS-derived debris map.

Both MODIS and MERIS Level-1B data were obtained from the NASA OB.DAAC (https://oceancolor.gsfc.nasa.gov) to generate Rayleigh-corrected reflectance (R_{rc}) in each spectral band (λ in nm) using the software SeaDAS (version 8.2, https://seadas.gsfc.nasa.gov). $R_{rc}(\lambda)$ data were used in three ways:

1) to compose false-color Red-Green-Blue (FRGB) images for a quick inspection of image features, where the 645-nm (665), 859-nm (865), and 469-nm (443) bands were used as the red, green, and blue channels, respectively. The wavelengths in the parentheses represent those of MERIS.
2) to analyze the spectral shapes of the identified image features, from which the type of floating matter can be inferred. The spectral shape of each randomly selected image feature pixel was determined from:

$$\Delta R_{rc}(\lambda) = {R_{rc}}^{T}(\lambda) - {R_{rc}}^{W}(\lambda) \quad (1)$$

$$= \left[\chi {R_{rc}}^{FM}(\lambda) + (1-\chi){R_{rc}}^{W}(\lambda)\right] - {R_{rc}}^{W}(\lambda) \quad (2)$$

$$= \chi\left({R_{rc}}^{FM}(\lambda) - {R_{rc}}^{W}(\lambda)\right) \quad (3)$$

$$= \chi\left(R^{FM}(\lambda) - R^{W}(\lambda)\right) \quad (4)$$

$$\approx \chi R^{FM}(\lambda) \left[\text{assuming } R^{W}(\lambda) \ll R^{FM}(\lambda) \text{ for } \lambda > 510 \text{ nm}\right], \quad (5)$$

where $\Delta R_{rc}(\lambda)$ is the difference between the image feature pixel ($R^{T}_{rc}(\lambda)$, where "T" stands for "target") and nearby water pixel ($R^{W}_{rc}(\lambda)$, where "W" stands for "water"). $R^{FM}(\lambda)$ is the reflectance of floating matter endmember, $R^{W}(\lambda)$ is the reflectance of water endmember, and χ (0–100 %) is the subpixel fraction of floating matter. Here, Eq. (2) is based on the linear mixing between floating matter and water within a pixel as they occupy fractions of χ and (1-χ), respectively, and Eq. (4) assumes that aerosol contributions to R_{rc} are the same between the target pixel and nearby water pixel. For clear waters and for $\lambda > 510$ nm, $R^{W}(\lambda)$ is mostly <0.01 (Lee et al., 2014), while $R^{FM}(\lambda)$ is >0.05 (Hu, 2021), thus leading to the approximation in Eq. (5). With χ being wavelength independent, the spectral shape of $\Delta R_{rc}(\lambda)$ is the same as $R^{FM}(\lambda)$ (Eq. (5)). Ttherefore, $\Delta R_{rc}(\lambda)$ can be used to infer the floating matter type from a spectral library of various types of floating matters.

3) to quantify floating matter in each image feature pixel, expressed as χ in Eq. (6):

$$\chi = \Delta R_{rc}(\text{NIR})/0.3. \quad (6)$$

Here, the unmixing equation is derived from Eq. (5) with the assumption of $R^{FM}(\text{NIR}) \approx 0.3$ for most floating matters including floating vegetation (Hu, 2021), plastics (Garaba and Dierssen, 2020), and driftwood (Song et al., 2021). The value of 0.3 represents the upper bound of reflectance with 100 % floating matter coverage within a pixel. Departure of the upper bound from the assumed 0.3 will result in a systematic bias (either underestimate or overestimate) in the estimated amount of floating matter but will not change either spatial distribution patterns or temporal changes. In this step, the image features were first delineated using a median filter applied to the NIR band (859 nm for MODIS, 250-m resolution), where each image feature pixel is referenced against the median value of the surrounding 11 × 11 pixels, with the difference being expressed as $\Delta R_{rc}(\text{NIR})$. Because the lower detection limit was estimated to be 1 % for sensors with signal-to-noise ratios (SNRs) of 200 such as the MODIS 250-m bands (Hu et al., 2015), a threshold of 1 % was used to delineate image features. The areal coverage of floating matter (in km^2) in an image was calculated as the integration of χ from all image features multiplied by the pixel size. The coverage was further converted to mass using a conversion factor of 200 kg m^{-2}, which assumed that the floating matter was neutrally buoyant

(i.e., its density is slightly less than water) with an average thickness of 20 cm. There is actually no knowledge from any field measurement about the thickness of floating debris after the 2011 tsunami, but considering the main debris types reported from the JTMD (polystyrene, wood, vessels, and construction materials) (Murray et al., 2018b) and from visual inspection of digital photos (https://www.bbc.com/news/world-asia-35638091; https://www.theguardian.com/world/2012/may/01/tsunami-japan-debris-us-canada), the assumption of 20 cm is reasonable. Departure from this value will cause a systematic bias in the mass estimation but will not impact either spatial patterns or temporal changes.

Landsat data were downloaded from the Google Earth Engine, from which FRGB images were generated and visually inspected to find image features. ASTER data in three spectral bands (520–600 nm, 630–690 nm, and 780–860 nm) were downloaded from LP.DAAC of the United States Geological Survey (USGS), and processed in the same way as MODIS using computer codes developed in house, where debris density was estimated using the NIR band in the same way as with MODIS.

3. Results

3.1. Initial distributions of JTMD

MODIS FRGB image sequence after the March 11 tsunami event revealed many anomalous image features, starting from Day 1 on March 12. An example is shown in Fig. 1a, where the FRGB image collected on Day 2 (March 13) reveals extensive image features, as illustrated in the zoom-in boxes in Fig. 1b & c, respectively. Here, the anomalous image features are defined as those greenish, elongated features that stand out from the background water (purple color in the FRGB images). They are different from clouds (white) or cloud shadows (dark). These image features occupy a narrow band of ~18 km E-W nearly parallel to the coast, spanning a N-S distance of ~380 km from 36.75°N to 40.25°N and mostly within 40 km of the shoreline. This suggests that the impact of the tsunami was extensive along the 380-km coast, a result consistent with the reported destroyed houses (Maximenko et al., 2018).

3.2. What type of marine debris?

While the greenish color shade of the FRGB image features is apparently due to enhanced NIR reflectance caused by solid materials on the water surface, analysis of MERIS-derived $\Delta R_{rc}(\lambda)$ spectral shapes suggests the possible type of the dominant debris. The MERIS $\Delta R_{rc}(\lambda)$ spectra from several randomly selected pixels of the greenish features in the MERIS FRGB images show monotonic increases from the blue to the NIR wavelengths, with $\Delta R_{rc}(\lambda)$ spectral shapes between 560 and 869 nm nearly parallel to each other (Fig. 2a & b). These spectral characteristics resemble those of driftwood reported after flooding events (Song et al., 2021; Hu, 2022), as shown by the gray-colored spectra. They also appear similar to the spectra of other types of wood (Todaro et al., 2012; Moshtaghi et al., 2021). Therefore, the dominant type of marine debris can be inferred to be some form of wood, and this inference is consistent with the report by the Ministry of Environment of Japan (MoE, 2012), where most marine debris was reported to be lumber wood of destroyed houses.

What is unknown is whether the detected marine debris contains other materials such as plastics. Unlike wood whose reflectance increases sharply from 560 nm to 705 nm (2–3 folds), the reflectance of plastics only increases slowly (~20 %) from 560 nm to 705 nm (Hu, 2021; Moshtaghi et al., 2021; Garaba and Dierssen, 2020). Therefore, from the reflectance spectral shape alone, it is clear that the dominant type of marine debris is not plastics. However, this does not rule out the possibility that a small portion of the detected debris is plastics as it is logical to infer plastics from damaged houses being washed off the coast, yet the portion cannot be determined from the spectral analysis here.

The same spectral analysis of MERIS was extended to MODIS, with results shown in Fig. 2c–d. Because of the lack of spectral bands, the inference of wood from the MODIS spectra is less definitive than that

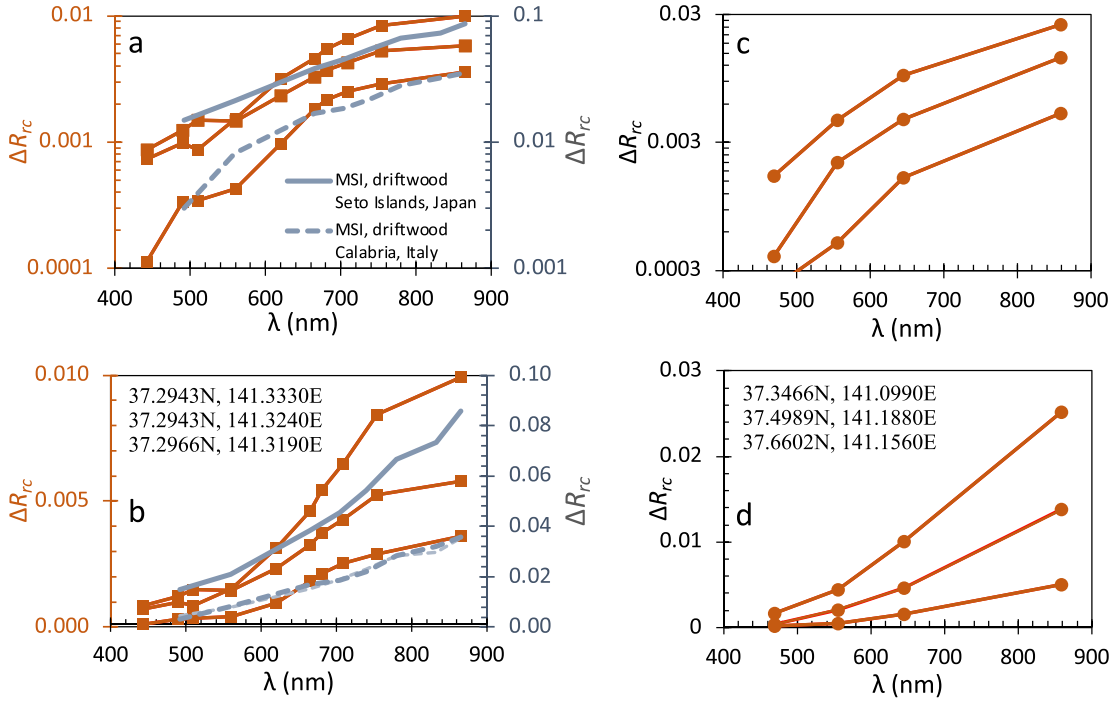

Fig. 2. Spectral characteristics of the image features captured in MERIS (a & b) and MODIS (c & d) images, respectively. (a) ΔR_{rc} spectra of 3 randomly selected pixels of image features from the MERIS image collected on 17 March 2011, together with the reference spectra of driftwood after flooding events in Japan and Italy (Song et al., 2021; Sannigrahi et al., 2022), (b) same spectra of (a) but plotted in linear scale (the locations of the three pixels are annotated), (c) ΔR_{rc} spectra of 3 randomly selected pixels of image features from the MODIS image collected on 12 March 2011, and (d) same spectra of (c) but plotted in linear scale (the locations of the three pixels are annotated).

from the MERIS spectra, yet the monotonic reflectance increases from 555 nm to 645 nm and then to 859 nm can still be used to infer solid materials. Such an inference is confirmed by the various field and airborne photos collected after the tsunami event (Murray et al., 2018b, and references therein).

3.3. How much?

Fig. 3a shows the debris areal density for the March 13 image, derived from the unmixing equation (Eq. (6)). To facilitate visualization, the 250-m pixels were binned to 2-km grids, where χ in each grid is an average of all valid pixels within the grid. Nearly all 2-km grids have <1 % of marine debris, suggesting the small size (relative to the size of MODIS pixels) and patchiness of marine debris. The aggregated areal coverage of marine debris (i.e., if all debris were put together to cover the water surface completely) is 7.6 km^2 from this image, corresponding to ~1.5 million metric tons under the assumed conversion factor of 200 kg m^{-2}. The data were further grouped to each 0.25° latitude interval from 36.75°N to 40.25°N and plotted along latitude (Fig. 3b). The debris showed an uneven distribution, with much more debris found to the south of 39°N where the latitudinal distribution down to 36.75°N is not uniform (Fig. 3b).

Sequential images revealed the temporal changes of marine debris distributions (Fig. 4). On Day 1 (March 12) after the tsunami, marine debris first appeared mostly to the south of 38°N. The maximal extent was found on Day 2 of March 13 (Fig. 3a). Then, most of the debris disappeared in just a few days in MODIS imagery, with total aggregated coverage of 6.4, 0.6, and 0.5 km^2 found on March 14, 18, and 19, respectively.

Inspection of the MODIS image sequence showed marine debris image features to at least March 28 (17 days after the tsunami event), after which MODIS images lost their capability to capture small patches of debris. However, inspection of the 30-m resolution Landsat image sequence, after zooming in every small region of the images, showed some small features (several pixels to tens of pixels) on April 6, after which no image features could be detected.

4. Discussions

4.1. Mapping accuracy

Other than sporadic digital photos to indirectly verify the image-based inference that the JTMD is dominated by wood, there is no direct ground measurement to validate such an inference, and nor can the estimates of areal coverage or mass be directly validated. This is actually a "traditional" problem for any remote sensing studies of floating matters including oil slicks and marine debris. There are several fundamental reasons behind this challenge: 1) it is difficult to measure the size and mass of a debris patch in the field; 2) it is difficult to relate the field measurement to the image pixel because the debris patch can change positions in less than 1 h; 3) even if the above two problems can be solved, it is still difficult to measure all debris patches in a large area in the field when evaluating the integrated areal coverage or mass from a satellite image.

However, the lack of direct field-based validation does not preclude our confidence in these remote sensing-based inference and estimates for two reasons. One, the reflectance spectral shape of wood is well distinguishable from all other reported floating matters including both vegetative (macroalgae mats and microalgae scums) and non-vegetative (plastic and non-plastic/non-wood debris) matters. The lack of the reflectance trough around 670 nm suggests that the image features are not caused by floating vegetations, and the sharp reflectance increase from 560 nm to 705 nm suggests that wood is the only plausible explanation. This is similar to imaging spectroscopy that is used to decipher the composition of the target. Two, similar to how other patchy floating matters can be indirectly validated, high-resolution images can be used to evaluate the accuracy of the density distributions derived from the medium-resolution images (Qi et al., 2023). Here, MODIS

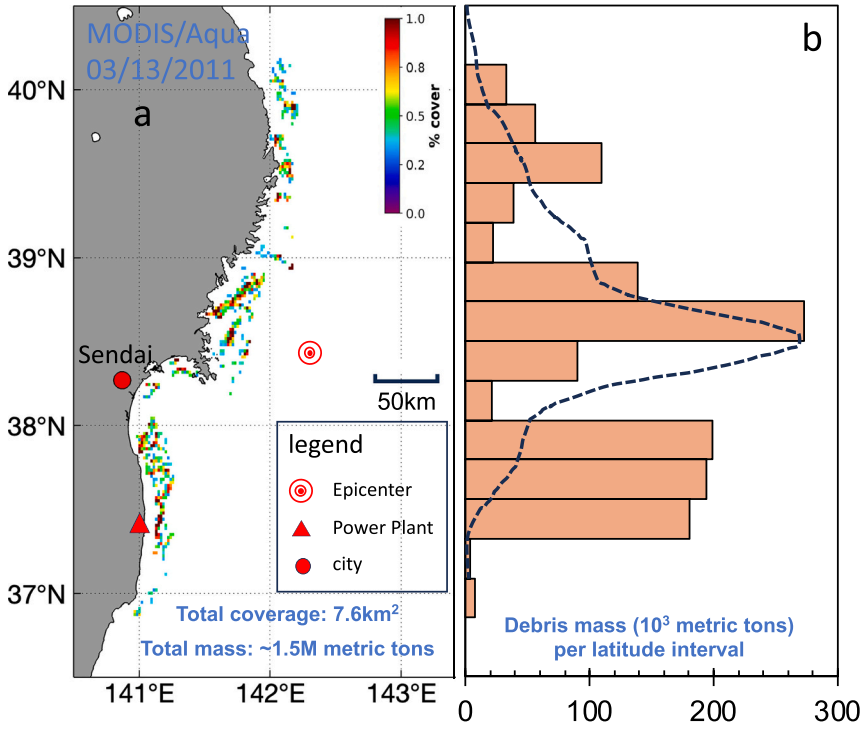

Fig. 3. (a) Distribution of marine debris density (percent cover in each 2-km grid cell) on 13 March 2011 corresponding to Fig. 1a. The total integrated debris coverage is annotated with land (dark gray), shoreline (black), and water (white). (b) Integrated debris mass between 36.5°N and 40.5°N is shown for each 0.25° in latitude, assuming 200 kg m^{-2} debris. Overlaid dashed curve is the assumed JTMD distribution along the coast to initialize a tracer model, adapted from Maximenko et al. (2018).

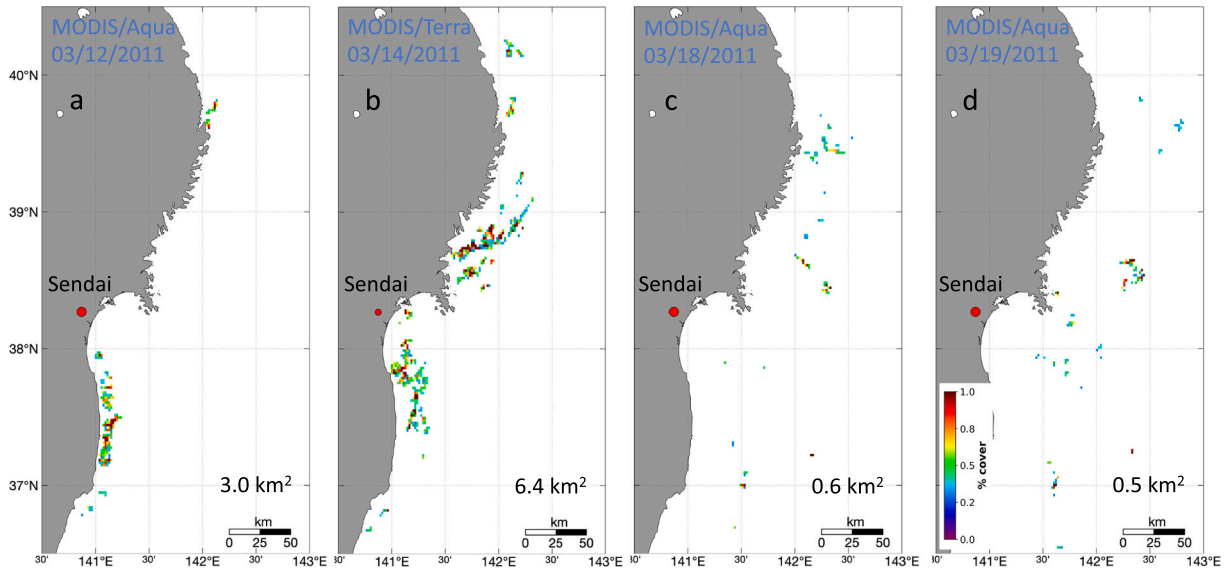

Fig. 4. Marine debris density maps derived from MODIS observations on March 12 (a), 14 (b), 18 (c), and 19 (c), respectively. The map for March 13 is presented in Fig. 3a. The density is expressed in percent cover of debris in each 2-km grid. The total integrated debris coverage is annotated in each map.

estimates of the JTMD distributions in a small area on March 14 are evaluated using the 15-m resolution ASTER image collected on the same day within 5 min (Fig. 5).

Within the same footprint of the ASTER image, MODIS-captured image features (Fig. 5b & d) are comparable to those captured by the ASTER image (Fig. 5c & e), with the latter being much clearer and sharper due to the much higher spatial resolution (15-m versus 250-m). A close inspection of the image pair suggests that some isolated small debris patches in the ASTER image are missed by the MODIS image, suggesting that high-resolution images would provide more accurate

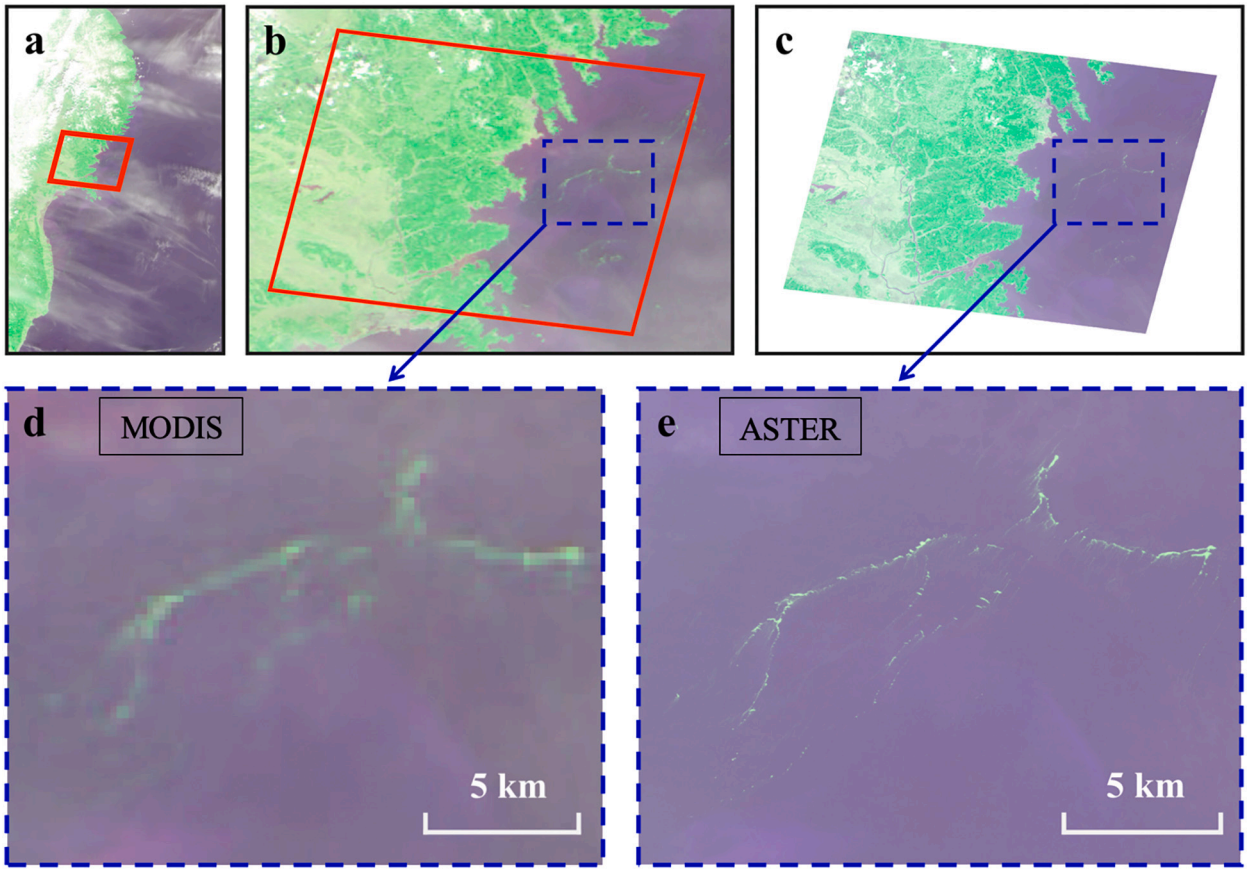

Fig. 5. Comparison between MODIS and ASTER observations of marine debris for (a) MODIS-Terra FRGB image (250-m resolution) on 14 March 2011 (01:15 GMT), with a subregion (red box) extracted in (b) to correspond to the ASTER footprint, and (c) ASTER FRGB image (15-m resolution) collected on the same day 5 min later (01:20 GMT). A small region outlined in the dashed rectangular box is enlarged in (d) and (e) to have a visual comparison of the greenish image features (marine debris). (For interpretation of the references to color in this figure legend, the reader is referred to the web version of this article.)

estimates of debris distributions if they were available more frequently with wider swaths. However, the debris density maps derived from both observations are very similar in both spatial distributions (Fig. 6a–c) and histogram statistics (Fig. 6d–f), suggesting the validity of the MODIS-based estimates in this study. This is primarily because of the pixel unmixing used in the areal estimates (Eq. (6)), but also because of the higher SNRs of MODIS to enable lower detection limit (Qi and Hu, 2021), a result consistent with those found in Qi et al. (2023).

Based on these evaluations, the MODIS-based estimates of JTMD distributions and areal coverage are believed to be relatively accurate although some small debris patches may be missed.

4.2. Strengths and limitations of the current remote sensing technique

The findings here were made possible through the use of multi-sensor remote sensing data as well as the techniques to spectrally discriminate floating matter type and to unmix mixed pixels. These sensors with different spatial, spectral, and temporal resolutions provide complementing advantages to map, discriminate, and quantify marine debris. The pixel subtraction technique in Eqs. (1)–(5) makes explicit atmospheric correction unnecessary because the atmospheric effect is mostly removed through the subtraction. Therefore, the technique can be applied to either surface reflectance, Rayleigh-corrected reflectance, or top-of-atmosphere (i.e., at-sensor) reflectance. Considering that the modern high-resolution sensors such as Sentinel-2 MSI (10–60 m, 5-day revisits) and PlanetScope Dove (or SuperDove) (~3 m, 1–2 day revisits) are not available prior to 2015, the capacity of the medium-resolution MODIS and MERIS is particularly important as they can be used to search and map large marine debris patches and other floating matters on a global scale (Qi et al., 2020). The use of sporadic Landsat and ASTER imagery is useful in detecting smaller debris patches and assessing uncertainties. Therefore, the remote sensing technique demonstrated here is especially useful in mapping debris after major disasters such as hurricanes and tsunamis (Hu et al., 2023). For more recent years, other medium-resolution sensors such as the Visible Infrared Imaging Radiometer Suite (VIIRS, 2011–present on SNPP, 2017–present on NOAA-20, and 2022–present on NOAA-21) and the Ocean and Land Colour Instrument (OLCI, 2016–present on Sentinel-3A and 2018–present on Sentinel-3B) can be paired in a similar fashion as pairing MODIS and MERIS to map large marine debris patches.

However, the technique is limited in its lack of combined spatial, temporal, and spectral resolutions in the same sensor to track small debris patches and to discriminate multiple types of debris in a given pixel. Ideally, a constellation of satellite sensors providing meter-scale resolution, near daily revisits, and hyperspectral shortwave infrared (SWIR) bands around 1200 nm and 1600 nm can significantly enhance the technique, as the absorption features of C-H bonds around those wavelengths can be used to fingerprint plastics (Garaba and Dierssen, 2020; Castagna et al., 2023). Because of the lack of such hyperspectral bands in this study, we can only infer the dominant debris type (wood, possibly lumber wood), although other types of debris such as plastics may coexist. Currently, some pathfinder missions (e.g., the Hyperspectral Precursor of the Application Mission (PRISMA) and the Earth Surface Mineral Dust Source Investigation (EMIT)) do provide such hyperspectral bands, yet considering their scarce measurements and relatively low SNRs, their capacity in discriminating debris types is still to be evaluated. Nevertheless, the modern sensors can significantly enhance our capability to monitor and track marine debris for event response and regional studies (e.g., Cózar et al., 2024). How to realize such a capability to conduct a systematic assessment at the global scale, however, remains to be investigated.

4.3. Implications

The findings here provide new information on the type, distribution, and amount of debris in the JTMD in the initial days after the tsunami event, which may assist in post-event damage assessment along the northeast coast of Japan and in the greater Pacific Ocean. Previous studies only used high-resolution satellite and airborne images to study the post-tsunami marine debris, which were restricted to small regions (e.g., a region of about 30 km in scale; yellow box in Fig. 1a) (Matthews et al., 2017). In contrast, this study revealed near-continuous

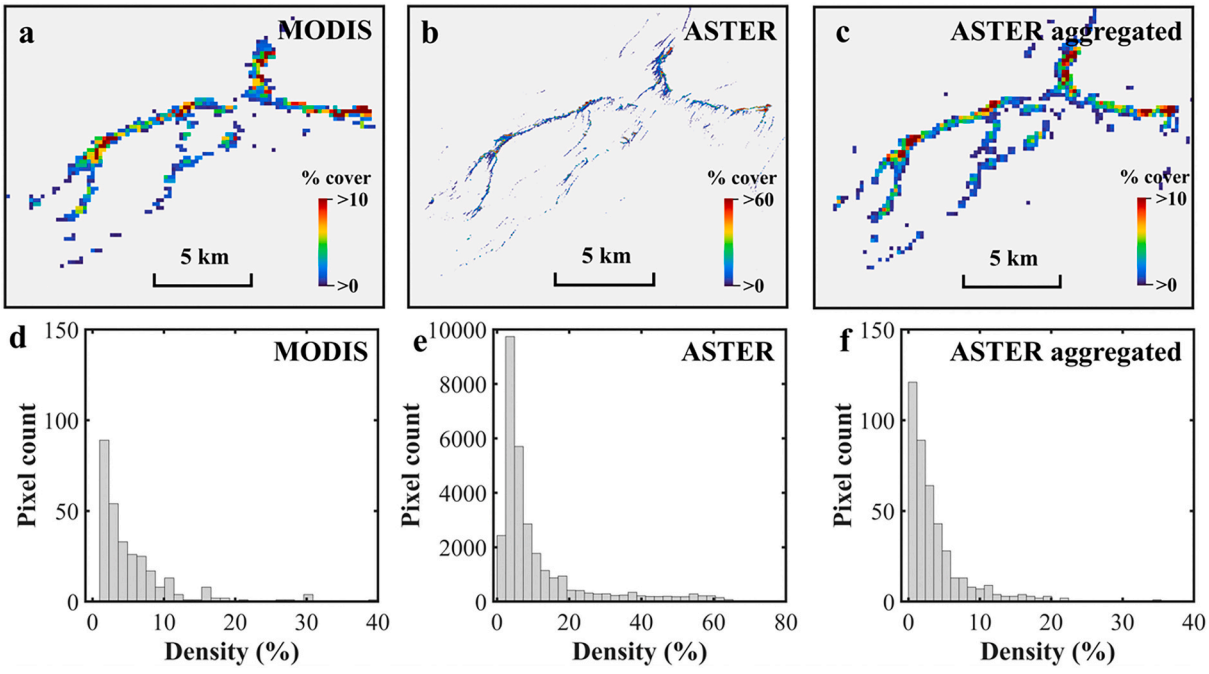

Fig. 6. Comparison of marine debris extraction results between MODIS (250-m resolution) and ASTER (15-m resolution) corresponding to Fig. 5d & c for (a) marine debris density in each 250-m MODIS image grid (14 March 2011, 01:15 GMT, see Fig. 5d), (b) marine debris density in each 15-m ASTER image grid (14 March 2011, 01:20 GMT, see Fig. 5e), and (c) same as in (b), but the data are aggregated to 250-m grid to compare with MODIS. The histogram distributions of all debris grids are presented in (d), (e), and (f), respectively.

distribution of the JTMD extending over 380 km along the northeast coast in an area of 6800 km^2 (Fig. 3a). The maximal aggregated debris area (7.6 km^2, Fig. 3a) is almost 30 times higher than that reported off the western Japan in July 2008 following a heavy flooding disaster (0.26 km^2, Song et al., 2021). Most of this debris disappeared in MODIS imagery in just a few days, suggesting possible sinking in this region. This information is useful in determining where to find the sinking debris and where to conduct the post-tsunami damage assessment in the extensive coastal areas as the debris may have a measurable and long-lasting impact on ocean ecology. In particular, because a lot of wood debris may have originated from the damaged houses where wood may be arsenic treated, these debris may be toxic to marine life (Weis and Weis, 1999). This is in addition to the potential risk induced by the invasive species found in the JTMD (Carlton et al., 2018; Hanyuda et al., 2018; Therriault et al., 2018). The information is also useful in refining numerical models to track the JTMD. For example, with little information on the initial JTMD distribution, the number of damaged houses along the coast was used as a surrogate to determine the relative number of debris particles to initialize a tracer model (Maximenko et al., 2018), with the relative particle distribution shown as the dashed curve in Fig. 3b. Comparing with the JTMD distribution determined from the MODIS image (horizontal bars in Fig. 3b), although the peak location in the simulated particle distribution is correct and the general north-south distribution is also reasonable, most of the debris to the south of the peak can be improved in the model initialization. How such a more realistic JTMD distribution, once used to re-initialize the model, will impact the outcome of the numerical tracer experiment, requires further research.

5. Conclusion

Thanks to the recent advances in methodology development, the information gap on the initial distributions of the Japanese Tsunami Marine Debris after the tragic tsunami event on 11 March 2011 is filled here using multi-sensor satellite data collected by MODIS, MERIS, ASTER, and Landsat. These sensors provide complementing advantages to map, discriminate, and quantify marine debris: MODIS has more frequent revisits suitable for mapping, MERIS has more spectral bands for spectral discrimination, ASTER has higher spatial resolution to understand uncertainties, and Landsat provides a compromise between spatial resolution and revisit to capture small debris patches. The findings here are useful for post-tsunami impact assessment in coastal waters off Northeast Japan and for refining numerical tracer models. The success is attributed to the combined use of multi-sensor remote sensing, the improved knowledge of reflectance spectral shapes of marine debris and other floating matters, and the practical approach to detect and quantify anomaly pixels. While the case study here demonstrates how to use multi-sensor satellite images to map marine debris after a major natural disaster, small debris patches may be missed due to the inherent sensor detection limitation. Such a limitation can be overcome with modern satellite sensors such as MSI (5-day revisits at 10 m resolution) and PlanetScope (1–2 day revisits at ~3 m resolution) for post-disaster debris assessment in the future.

CRediT authorship contribution statement

Lin Qi: Writing – review & editing, Writing – original draft, Visualization, Methodology, Investigation. **Menghua Wang:** Writing – review & editing, Writing – original draft, Supervision, Funding acquisition. **Chuanmin Hu:** Writing – review & editing, Writing – original draft, Visualization, Supervision, Methodology, Conceptualization. **Junnan Jiao:** Visualization, Methodology, Investigation, Data curation. **Young-Je Park:** Writing – review & editing, Writing – original draft, Resources, Methodology, Data curation.

Declaration of competing interest

The authors declare that they have no known competing financial interests or personal relationships that could have appeared to influence the work reported in this paper.

Data availability

Data will be made available on request.

Acknowledgements

This work was supported by the U.S. Joint Polar Satellite System (JPSS) program (ST13301CQ0050/1332KP22FNEED0042) and NASA through its Ocean Biology and Biogeochemistry program and Ecological Forecast program (80NSSC20M0264, 80NSSC21K0422, 80NSSC24K1507). We thank NASA and the European Space Agency for providing MODIS and MERIS data, respectively. We thank the U.S. Geological Survey for providing Landsat and ASTER data. We also thank the editor and three anonymous reviewers for their prompt feedback on how to improve the presentation of this work. The scientific results and conclusions, as well as any views or opinions expressed herein, are those of the authors and do not necessarily reflect those of NOAA or the Department of Commerce.

References

Arii, M., Koiwa, M., Aoki, Y., 2014. Applicability of SAR to marine debris surveillance after the Great East Japan Earthquake. IEEE J. Sel. Top. Appl. Earth Obs. Remote Sens. 7 (5), 1729–1744. https://doi.org/10.1109/JSTARS.2014.2308550.

Battisti, C., Staffieri, E., Peota, G., Sorace, A., Luiselli, L., Amori, G., 2019. Interactions between anthropogenic litter and birds: a global review with a 'black-list' of species. Mar. Pollut. Bull. 138, 93–114. https://doi.org/10.1016/j.marpolbul.2018.11.017.

Carlton, J.T., Chapman, J.W., Geller, J.B., Miller, J.A., Carlton, D.A., McCuller, M.I., Treneman, N.C., Steves, B.P., Ruiz, G.M., 2017. Tsunami-driven rafting: transoceanic species dispersal and implications for marine biogeography. Science 357 (6358), 1402–1406.

Carlton, J.T., Chapman, J.W., Geller, J.B., Miller, J.A., Ruiz, G.M., Carlton, D.A., McCuller, M.I., Treneman, N.C., Steves, B.P., Breitenstein, R.A., Lewis, R., Bilderback, D., Bilderback, D., Haga, T., Harris, L.H., 2018. Ecological and biological studies of ocean rafting: Japanese tsunami debris arriving in North America and the Hawaiian Islands between 2012 and 2017. Aquat. Invasions 13, 1–9. https://doi.org/10.3391/ai.2018.13.1.01.

Castagna, A., Dierssen, H.M., Devriese, L.I., Everaert, G., Knaeps, E., Sterckx, S., 2023. Evaluation of historic and new detection algorithms for different types of plastics over land and water from hyperspectral data and imagery. Remote Sens. Environ. 298, 113834 https://doi.org/10.1016/j.rse.2023.113834.

Cózar, A., Echevarría, F., González-Gordillo, J.I., Irigoien, X., Úbeda, B., Hernández-León, S., Palma, Á.T., Navarro, S., García-de-Lomas, J., Ruiz, A., Fernández-de-Puelles, M.L., Duarte, C.M., 2014. Plastic debris in the open ocean. Proc. Natl. Acad. Sci. 111 (28), 10239–10244.

Cózar, A.M., Arias, G., Suaria, G., et al., 2024. Proof of concept for a new sensor to monitor marine litter from space. Nat. Commun. 15, 4637. https://doi.org/10.1038/s41467-024-48674-7.

Eriksen, M., Lebreton, L.C., Carson, H.S., Thiel, M., Moore, C.J., Borerro, J.C., Galgani, F., Ryan, P.G., Reisser, J., 2014. Plastic pollution in the world's oceans: more than 5 trillion plastic pieces weighing over 250,000 tons afloat at sea. PLoS One 9 (12), e111913.

Fujii, Y., Satake, K., Sakai, S., et al., 2011. Tsunami source of the 2011 off the Pacific coast of Tohoku Earthquake. Earth Planets Space 63, 815–820. https://doi.org/10.5047/eps.2011.06.010.

Garaba, S.P., Dierssen, H.M., 2020. Hyperspectral ultraviolet to shortwave infrared characteristics of marine-harvested, washed-ashore and virgin plastics. Earth Syst. Sci. Data 12 (1), 77–86.

Goddijn-Murphy, L., Martínez-Vicente, V., Dierssen, H.M., Raimondi, V., Gandini, E., Foster, R., Chirayath, V., 2024. Emerging technologies for remote sensing of floating and submerged plastic litter. Remote Sens. 16, 1770. https://doi.org/10.3390/rs16101770.

Hanyuda, T., Hansen, G.I., Kawai, H., 2018. Genetic identification of macroalgal species on Japanese tsunami marine debris and genetic comparisons with their wild populations. Mar. Pollut. Bull. 132, 74–81. https://doi.org/10.1016/j.marpolbul.2017.06.053.

Hu, C., 2021. Remote detection of marine debris using satellite observations in the visible and near infrared spectral range: challenges and potentials. Remote Sens. Environ. 259, 112414.

Hu, C., 2022. Remote detection of marine debris using Sentinel-2 imagery: a cautious note on spectral interpretations. Mar. Pollut. Bull. 183, 114082.

Hu, C., Feng, L., Hardy, R.F., Hochberg, E.J., 2015. Spectral and spatial requirements of remote measurements of pelagic Sargassum macroalgae. Remote Sens. Environ. 167, 229–246.

Hu, C., Qi, L., Wang, M., Park, Y.-J., 2023. Floating debris in the northern Gulf of Mexico after hurricane Katrina. Environ. Sci. Technol. 57, 10373–10381. https://doi.org/10.1021/acs.est.3c01689.

Kikaki, K., Kakogeorgiou, K.I., Hoteit, I., Karantzalos, K., 2024. Detecting marine pollutants and sea surface features with deep learning in Sentinel-2 imagery. ISPRS J. Photogramm. Remote Sens. 210, 39–54.

Law, K.L., Morét-Ferguson, S., Maximenko, N.A., Proskurowski, G., Peacock, E.E., Hafner, J., Reddy, C.M., 2010. Plastic accumulation in the North Atlantic subtropical gyre. Science 329 (5996), 1185–1188.

Lee, Z., Shang, S., Hu, C., Zibordi, G., 2014. Spectral interdependence of remote-sensing reflectance and its implications on the design of ocean color satellite sensors. Appl. Opt. 53, 3301–3310.

MacLeod, M., Arp, H.P.H., Tekman, M.B., Jahnke, A., 2021. The global threat from plastic pollution. Science 373 (6550), 61–65.

Martínez-Vicente, V., Clark, J.R., Corradi, P., Aliani, S., Arias, M., Bochow, M., Bonnery, G., Cole, M., Cózar, A., Donnelly, R., Echevarría, F., Galgani, F., Garaba, S. P., Goddijn-Murphy, L., Lebreton, L., Leslie, H.A., Lindeque, P.K., Maximenko, N., Martin-Lauzer, F.-R., Moller, D., Murphy, P., Palombi, L., Raimondi, V., Reisser, J., Romero, L., Simis, S.G.H., Sterckx, S., Thompson, R.C., Topouzelis, K.N., van Sebille, E., Veiga, J.M., Vethaak, A.D., 2019. Measuring marine plastic debris from space: initial assessment of observation requirements. Remote Sens. 11 (20), 2443.

Matthews, J.P., Ostrovsky, L., Yoshikawa, Y., Komori, S., Tamura, H., 2017. Dynamics and early post-tsunami evolution of floating marine debris near Fukushima Daiichi. Nat. Geosci. 10 (8), 598–603.

Maximenko, N., Hafner, J., Kamachi, M., MacFadyen, A., 2018. Numerical simulations of debris drift from the Great Japan Tsunami of 2011 T and their verification with observational reports. Mar. Pollut. Bull. 132, 5–25.

Ministry of Environment of Japan (MoE), 2012. Estimated total amount of debris washed out by the Great East Japan Earthquake. http://www.env.go.jp/en/focus/docs/files/20120901-57.pdf. (Accessed 15 March 2023).

Moshtaghi, M., Knaeps, E., Sterckx, S., Garaba, S., Meire, D., 2021. Spectral reflectance of marine macroplastics in the VNIR and SWIR measured in a controlled environment. Sci. Rep. 11 (1), 5436.

Murray, C.C., Maximenko, N., Lippiatt, S., 2018a. The influx of marine debris from the Great Japan Tsunami of 2011 to North American shorelines. Mar. Pollut. Bull. 132, 26–32.

Murray, C.C., Therriault, T.W., Maki, H., Wallace, N., Carlton, J.T., Bychkov, A., 2018b. ADRIFT in the North Pacific: the movement, surveillance, and impact of Japanese tsunami debris. Mar. Pollut. Bull. 132, 1–4. https://doi.org/10.1016/j.marpolbul.2018.06.040.

Poeta, G., Staffieri, E., Acosta, A.T.R., Battisti, C., 2017. Ecological effects of anthropogenic litter on marine mammals: a global review with a "black-list" of impacted taxa. Hystrix 28 (2), 253–264.

Qi, L., Hu, C., 2021. To what extent can Ulva and Sargassum be detected and separated in satellite imagery? Harmful Algae 103, 102001. https://doi.org/10.1016/j.hal.2021.102001.

Qi, L., Hu, C., Mikelsons, K., Wang, M., Lance, V., Sun, S., Barnes, B.B., Zhao, J., Van der Zande, D., 2020. In search of floating algae and other organisms in global oceans and lakes. Remote Sens. Environ. 239, 111659.

Qi, L., Wang, M., Hu, C., 2023. Uncertainties in MODIS-derived Ulva prolifera amounts in the Yellow Sea: a systematic evaluation using Sentinel-2/MSI observations. IEEE Geosci. Remote Sens. Lett. 20, 1501805 https://doi.org/10.1109/LGRS.2023.3272889.

Sannigrahi, S., Basu, B., Basu, A.S., Pilla, F., 2022. Development of automated marine floating plastic detection system using Sentinel-2 imagery and machine learning models. Mar. Pollut. Bull. 178, 113527.

Song, S., Sakuno, Y., Taniguchi, N., Iwashita, H., 2021. Reproduction of the marine debris distribution in the Seto Inland Sea immediately after the July 2018 heavy rains in Western Japan using multidate Landsat-8 Data. Remote Sens. 13 (24), 5048.

Staffieri, E., de Lucia, G.A., Camedda, A., Poeta, G., Battisti, C., 2019. Pressure and impact of anthropogenic litter on marine and estuarine reptiles: an updated blacklist highlighting gaps of evidence. Environ. Sci. Pollut. Res. 26, 1238–1249. https://doi.org/10.1007/s11356-018-3616-4.

Suppasri, A., Shuto, N., Imamura, F., et al., 2013. Lessons learned from the 2011 Great East Japan tsunami: performance of tsunami countermeasures, coastal buildings, and tsunami evacuation in Japan. Pure Appl. Geophys. 170, 993–1018. https://doi.org/10.1007/s00024-012-0511-7.

Themistocleous, K., Papoutsa, C., Michaelides, S., Hadjimitsis, D., 2020. Investigating detection of floating plastic litter from space using sentinel-2 imagery. Remote Sens. 12 (16), 2648.

Therriault, T.W., Nelson, J.C., Carlton, J.T., Liggan, L., Otani, M., Kawai, H., Scriven, D., Ruiz, G.M., Murray, C.C., 2018. The invasion risk of species associated with Japanese Tsunami Marine T Debris in Pacific North America and Hawaii. Mar. Pollut. Bull. 132, 82–89. https://doi.org/10.1016/j.marpolbul.2017.12.063.

Todaro, L., Zuccaro, L., Marra, M., Basso, B., Scopa, A., 2012. Steaming effects on selected wood properties of Turkey oak by spectral analysis. Wood Sci. Technol. 46 (1), 89–100.

Topouzelis, K., Papageorgiou, D., Suaria, G., Aliani, S., 2021. Floating marine litter detection algorithms and techniques using optical remote sensing data: a review. Mar. Pollut. Bull. 170, 112675.

Weis, P., Weis, J., 1999. Accumulation of metals in consumers associated with chromated copper arsenate-treated wood panels. Mar. Environ. Res. 48, 73–81.